In operando study of orthorhombic V_2O_5 as positive electrode materials for K-ion batteries

Qiang Fu [a],[*], Angelina Sarapulova [a], Lihua Zhu [a], Georgian Melinte [b],[c], Alexander Missyul [d], Edmund Welter [e], Xianlin Luo [a], Michael Knapp [a],[b], Helmut Ehrenberg [a],[b], Sonia Dsoke [a],[b]

[a] *Institute for Applied Materials (IAM), Karlsruhe Institute of Technology (KIT), Hermann-von-Helmholtz-Platz 1, D-76344 Eggenstein-Leopoldshafen, Germany*
[b] *Helmholtz Institute Ulm for Electrochemical Energy Storage (HIU), Helmholtzstrasse 11, 89081 Ulm, Germany*
[c] *Institute of Nanotechnology (INT), Karlsruhe Institute of Technology (KIT), Hermann-von-Helmholtz-Platz 1, D-76344 Eggenstein-Leopoldshafen, Germany*
[d] *CELLS-ALBA Synchrotron, E-08290 Cerdanyola del Valles, Barcelona, Spain*
[e] *Deutsches Elektronen-Synchrotron DESY, Notkestraße 85, D-22607 Hamburg, Germany*

ARTICLE INFO

ABSTRACT

Herein, the electrochemical performance and the mechanism of potassium insertion/deinsertion in orthorhombic V_2O_5 nanoparticles are studied. The V_2O_5 electrode displays an initial potassiation/depotassiation capacity of 200 mAh g^{-1}/217 mAh g^{-1} in the voltage range 1.5–4.0 V vs. K^+/K at C/12 rate, suggesting fast kinetics for potassium insertion/deinsertion. However, the capacity quickly fades during cycling, reaching 54 mAh g^{-1} at the 31st cycle. Afterwards, the capacity slowly increases up to 80 mAh g^{-1} at the 200th cycle. The storage mechanism upon K ions insertion into V_2O_5 is elucidated. *In operando* synchrotron diffraction reveals that V_2O_5 first undergoes a solid solution to form $K_{0.6}V_2O_5$ phase and then, upon further K ions insertion, it reveals coexistence of a solid solution and a two-phase reaction. During K ions deinsertion, the coexistence of solid solution and the two-phase reaction is identified together with an irreversible process. *In operando* XAS confirms the reduction/oxidation of vanadium during the K insertion/extraction with some irreversible contributions. This is consistent with the results obtained from synchrotron diffraction, *ex situ* Raman, X-ray photoelectron spectroscopy (XPS), and transmission electron microscopy (TEM). Moreover, *ex situ* XPS confirms the "cathode electrolyte interphase" (CEI) formation on the electrode and the decomposition of CEI film during cycling.

1. Introduction

Along with their rapid development in modern society, renewable energy sources, such as solar, wind, geothermal power, and biomass energy, are playing crucial roles as power supplies. In particular, solar and wind powers gradually take an increasing share in energy supply. However, they are inherently intermittent and generally dispersed, strongly depending on the weather, time, and season, as well as location, while the consumption and demands of electric energy are comparatively constant [1]. Therefore, rechargeable batteries, being large-scale electrochemical energy storage systems (EESs), are necessary to realize the smooth integration of these intermittent energies into grids [2].

The first rechargeable potassium battery concept was designed by Eftekhari [3] in 2004, who employed Prussian blue (PB) positive electrode and potassium metal within 1 M KBF_4 in 3:7 of ethylene carbonate (EC):ethylmethyl carbonate (EMC) as electrolyte. Since then, potassium-ion batteries (KIBs) are becoming promising candidates to replace lithium-ion batteries (LIBs) for large-scale EESs. One of the main advantages is the abundance and low cost of potassium. Moreover, even if the K-ion is larger and heavier than Li^+, Na^+, and Mg^{2+}, the K^+/K couple has a standard electrode potential (-2.936 V vs. SHE) lower than that of Na^+/Na (-2.714 V vs. SHE) and Mg^{2+}/Mg (-2.37 V vs. SHE) [4]. Considering the gravimetric capacity, it is not appropriate just to compare the atomic weight of metals to calculate it. Instead, one should compare the formula weight of electrode materials as stated by Komaba et al. [5]. For example, the mass ratio of (P2-type $K_{2/3}CoO_2$):(O3-$LiCoO_2$) is 1.19, giving a 19% increase of the positive electrode material mass despite that the K atom is 5.7 times heavier than Li (M_K:M_{Li} = 39/6.

9 = 5.7). Therefore, the usage of heavier alkali elements (Na, Mg, and K) does not significantly influence the total weight of the battery. In addition, K-ion in propylene carbonate (PC) displays a lower ion–solvent interaction due to a lower desolvation energy and a smaller solvated ion compared to Li- and Na-ion, resulting in fast diffusion kinetics and high rate capability [6]. Another advantage is that Al can be used as the current collector in anodes for both sodium-ion batteries (SIBs) and KIBs, whereas an expensive and heavier Cu foil must be used in anodes for LIBs, due to the Li-Al alloy formation at low potential [7,8]. Moreover, the fact that graphite electrodes can deliver a high reversible capacity of 279 mAh g^{-1}, with the formation of KC_8 [9], makes KIBs more advantageous than SIBs, where graphite cannot be used. Recently, other materials such as soft and hard carbon, Ti-based materials, transition metal sulfides, black P and organic compounds are also reported as negative electrodes for KIBs [10,11]. However, due to the large ionic radius of K$^+$ (1.38 Å), KIBs are still in their infancy and facing big challenges to develop electrode materials suitable for commercialization. To date, only limited positive electrode materials have been reported, including Prussian blue analogous, polyanionic, and organic compounds, as well as layered material (Co-, Mn-, Cr-, and V-based oxides) [10,11]. Among them, the V-based oxides are very promising for the application in KIBs. For example, Clites and co-workers [12] recently reported that δ-$K_xV_2O_5 \cdot nH_2O$ positive electrode with an interlayer spacing of 9.65 Å shows good electrochemical performance towards K-insertion/deinsertion with an initial potassiation capacity of 268 mAh g^{-1} at C/50 and of 226 mAh g^{-1} at C/15 rate in the potential range of 2.0–4.3 V vs. K$^+$/K. The layered $K_{0.5}V_2O_5$, investigated by Deng et al. [13], delivers a reversible capacity of 90 mAh g^{-1} at a current density of 10 mA g^{-1} and displays capacity retention of around 80% after 250 cycles at 100 mA g^{-1} in the potential range of 1.5–3.8 V vs. K$^+$/K. *Ex situ* X-ray diffraction (XRD) and X-ray photoelectron spectroscopy (XPS) demonstrate that $K_{0.5}V_2O_5$ is highly stable, undergoing reversible structural changes during K-ions insertion and extraction. Zhu et al. [14] reported a bilayered δ-$K_{0.51}V_2O_5$ positive electrode, which shows a capacity of 131 mAh g^{-1} with excellent rate capability and a high average voltage of 3.2 V. A $V_2O_5 \cdot 0.6H_2O$ xerogel positive electrode, which was reported by Tian et al. [15], delivers an initial potassiation capacity of 224 mAh g^{-1} at 50 mA g^{-1} with a value of 103 mAh g^{-1} after 500 cycles in the potential range 1.5–4.0 V vs. K$^+$/K. Zhang et al. [16] reported a new layered compound orthorhombic $K_{0.83}V_2O_5$ with space group of *Pnma*, delivering an initial depotassiation/potassiation capacity of 86/90 mAh g^{-1} with a plateau of 3.5 V (vs. K$^+$/K) and high capacity retention of 80% over 200 cycles.

Orthorhombic layered V_2O_5 materials are intensively studied as a model system for intercalaction, but only few works focus on a study of these materials in KIBs. For example, in a work related to the $V_2O_5 \cdot 0.6H_2O$ xerogel, Tian et al. [15] reported on the performance of crystalline V_2O_5. However, this material displays a potassiation insertion capacity of only 44.3 mAh g^{-1} at 50 mA g^{-1}. Very recently, Ye and co-authors [17] reported on an amorphous V_2O_5/carbon nanotube sponge with an initial potassiation capacity of 206 mAh g^{-1} at 5 mA g^{-1}. However, the observed capacities are much lower than the theoretical capacity of 295 mAh g^{-1} (calculated considering 2 K-ions insertion) and no detailed K-storage mechanism of V_2O_5 is proposed up to now.

In operando synchrotron powder diffraction and *in operando* X-ray absorption spectroscopy (XAS) are very powerful tools to uncover the evolution of long- and short-range crystal structures and oxidation states of the transition metals during the electrochemical reactions [18]. The extremely bright, high flux, and high-energy synchrotron radiation provides many advantages for *in operando* studies in battery materials, for example, (1) the easy penetration through the sample, (2) high-quality data, (3) providing a "real-time study" of time-dependent reactions.

In operando synchrotron diffraction and *in operando* XAS have not yet been employed to look into the detailed storage mechanism of α-V_2O_5 in KIBs. As demonstrated by first-principles calculations, the migration barrier for K$^+$ in a monolayer of V_2O_5 is reduced to 0.39 eV, which is much lower than in bulk V_2O_5 (1.66 eV) [19,20]. Therefore, in our work, nanostructured V_2O_5 materials are prepared to potentially enhance the electrochemical activity of V_2O_5 positive electrode and to investigate the reaction mechanism during cycling. The present work focuses on the investigation of the electrochemical properties of V_2O_5 nanoparticles in 1 M KPF$_6$/PC and its storage mechanism during K ions insertion and extraction by *in operando* synchrotron diffraction and *in operando* XAS.

2. Experimental

2.1. Synthesis of V_2O_5 nanoparticles

The V_2O_5 nanoparticles were synthesized through a hydrothermal method. Typically, 1.0 mL of 2 M HCl, 0.3 g of ammonium metavanadate (NH$_4$VO$_3$), and 0.5 g of surfactant P123 (EO$_{20}$PO$_{70}$-EO$_{20}$, where EO and PO represent ethylene oxide and propylene oxide, respectively) purchased from Sigma Aldrich were mixed into 30 mL of deionized water under ultrasonication for 10 min and then under stirring for 1 h. After that, the mixed solution was transferred to 50 mL Teflon-lined autoclaves and maintained at 120 °C for 24 h with intermittent stirring in an oven. The resulting precipitate was filtered and washed with water and acetone several times, then dried under vacuum at 120 °C for 24 h. The product was annealed at 400 °C for 2 h in air after heating with a rate of 10 °C/min.

2.2. Preparation of electrolyte

The preparation of the electrolyte was carried out in a glovebox (MBraun) under Ar atmosphere with very low H$_2$O and O$_2$ content (<2 ppm). 1 M KPF$_6$/PC electrolyte was prepared by dissolving a corresponding amount of KPF$_6$ powder in PC under vigorous stirring at room temperature in the glovebox. All chemicals are battery grade and purchased from Sigma-Aldrich.

2.3. Morphological and structural study

The morphology was studied with a Zeiss Supra 55 scanning electron microscope (SEM) with primary energy of 15 keV. The structural characterizations were done using synchrotron radiation (λ = 0.4131 Å, 30 keV) at the Material Science and Powder Diffraction beamline (MSPD) at the ALBA synchrotron source (Barcelona, Spain) [21]. The powder diffraction patterns were measured in capillary geometry with powders filled in 0.5 mm Ø boro-silicate capillaries. A LabRam HR Evolution Raman microscope from Horiba Scientific equipped with HeNe laser (633 nm, 17 mW) and a CCD detector (Horiba) was used to collect the Raman scattering of the samples. Meanwhile, a 600 grating was used to split the measurement signal with a x 100 objective (NA 0.95) for all the pristine and cycled samples. The data was collected for 30 s with 4.25 mV of the laser and five measurements were added to reduce signal noise. In addition, the potassiated and depotassiated electrodes were sealed in an *in situ* Raman cell with a quartz window inside a glovebox. For transmission electron microscopy (TEM), all samples were pre-

pared under an argon atmosphere inside a glovebox. The samples dispersed onto a carbon-coated grid by dry powder deposition were transferred to the TEM by using a Gatan TEM vacuum transfer holder. The TEM samples were examined using a Titan 80–300 electron microscope (FEI), equipped with a CEOS image spherical aberration corrector, high angle annular dark field (HAADF) scanning transmission electron microscopy (STEM) detector and a Tridiem Gatan image filter (GIF). The microscope was operated at an accelerating voltage of 300 kV. X-ray photoelectron spectroscopy measurements were performed using a K-Alpha$^+$ XPS spectrometer (ThermoFisher Scientific, East Grinstead, UK), applying a microfocused, monochromated Al K_α X-ray source with a spot size of 400 μm. The sample storage and transportation were done in an airtight transport vessel under Ar to the spectrometer. To prevent any localized charge buildup, the K-Alpha$^+$ charge compensation system was employed during analysis, using electrons of 8 eV energy and low-energy argon ions. The Thermo Avantage software was used for data acquisition and processing [22]. The spectra were fitted with one or more Voigt profiles (binding energy uncertainty: ±0.2 eV). All spectra were referenced to the O 1s peak of vanadium oxide at 530.0 eV binding energy controlled by means of the well-known photoelectron peaks of metallic Cu, Ag, and Au.

2.4. Electrochemical characterization

The electrode slurry/mixture was prepared by mixing the active material (consisting of V_2O_5 nanoparticles) with Super C65 (TIMCAL) and polyvinylidene difluoride (PVDF) binder in a weight ratio of 70:20:10 with N-methyl-2-pyrrolidone solvent. The slurry was coated on 15 μm thick Al foil and dried at 70 °C overnight. The electrodes (1 mg cm^{-2}) were cut into discs with 12 mm diameter and then dried in the vacuum oven at 110 °C for 12 h. Electrochemical performance was studied in 2032-type coin cells using potassium as the negative and V_2O_5 as the positive electrode with Whatman separator in 1 M KPF$_6$/PC electrolyte. The cells were assembled in a glovebox filled with Ar. Galvanostatic cycling experiments were conducted with a rate of C/12 on a multichannel electrochemical workstation (Bio-Logic VMP). For ex $situ$ Raman and XPS, the cells were disassembled after cycling and the electrodes washed with PC in an Ar-filled glovebox. These samples consist of a V_2O_5 electrode potassiated one time at a lower cut-off voltage of 1.5 V and a sample first potassiated and then depotassiated one time at an upper cut-off voltage of 4.0 V with C/12 rate.

2.5. In operando synchrotron diffraction and in operando XAS

In $operando$ synchrotron diffraction was performed at the Material Science and Powder Diffraction beamline (MSPD) at the ALBA synchrotron. The in $operando$ cells were built using 2025-type coin cells with glass windows of 5 mm diameter beam entrance. The positive electrode (active materials, 2 mg, and ∼ 7 mg cm^{-2}) was prepared by pressing the electrode mixture on Al mesh within a 5 mm hole in the center, and K negative electrode with a 5 mm hole in the center. More details of this setup can be found elsewhere [23]. In $operando$ synchrotron diffraction data were collected at room temperature with radiation λ = 0.4131 Å wavelength (30 keV) and position sensitive detector MYTHEN. Data were collected with an effective exposure time of 60 s in steps of 0.006° over the angular range of 1.8°–42° in 2theta during the first cycles with C/15 rate (cell was running at a rate of C/30 for the first 5.4 h). The coin cells were continuously oscillated ±5° around the incoming beam direction to improve the powder averaging (increasing the number of crystallites contribution). The diffraction data analysis was carried out by the Rietveld method

using the Fullprof software package. In $operando$ XAS measurements were performed at the synchrotron beamline P65 at PETRA III (DESY, Hamburg). Electrochemical cycling was conducted in 2025-type coin cell with 5 mm-diameter Kapton window for the first potassiated-depotassiated processes with C/14 rate. XAS spectra at the V K-edge were recorded in quick-XAS (6 min/spectrum) mode in fluorescence geometry using a PIPS (passivated implanted planar silicon) diode. The V K-edge for V_2O_5 was measured for the 1st cycle and the energy was calibrated utilizing a vanadium foil as commonly applied in XAS experiments. V_2O_3, VO_2, and V_2O_5 were used as reference materials for V^{3+}, V^{4+} and V^{5+}, respectively. All the data were collected at room temperature with a Si(1 1 1) double crystal monochromator and all the XAS spectra were processed using the DEMETER software package.

3. Results and discussion

3.1. Structural and morphological characterization

Fig. 1(a) displays the synchrotron diffraction pattern of pristine V_2O_5 nanoparticles, suggesting a high crystallinity of V_2O_5 nanoparticles. All reflections can be indexed in the orthorhombic α-V_2O_5 with space group $Pmn2_1$, and the lattice parameters are a = 11.509(1) Å, b = 4.374(1) Å, and c = 3.564(1) Å (Table S1), consistent with reported work [24]. Note that the common space group for pristine α-V_2O_5 is $Pmmn$ [25]. Actually, both space groups $Pmn2_1$ and $Pmmn$ belong to the orthorhombic system. $Pmn2_1$ is acentric, while $Pmmn$ is centrosymmetric because of the existence of additional inversion symmetry in $Pmmn$. Rietveld refinement based on both models demonstrated that a smaller Chi and R_f-factor can be observed when acentric space group is used (Fig. S1, Tables S1–S3), suggesting it is more reasonable when acentric $Pmn2_1$ is used. It is impossible to distinguish the two space groups via X-ray powder diffraction analysis and we prefer to use $Pmn2_1$ because of the sigle crystal results by Novák et al. [24]. Moreover, b-axes is perpendicular to the [VO$_5$] square pyramids layer of V_2O_5 in space group $Pmn2_1$, while c-axes is perpendicular to that of V_2O_5 in space group $Pmmn$ (Fig. S1). Rietveld refinement shows the average apparent size of 62 nm with a standard deviation of 33 nm. Scanning electron microscopy (SEM) in Fig. 1(b) confirms that the V_2O_5 consists of nanoparticles (around 50–200 nm), in agreement with Rietveld refinement result.

3.2. Electrochemical properties

Fig. 2(a) displays the potential-capacity curves of V_2O_5 nanoparticles electrode in 1 M KPF$_6$/PC electrolyte cycled with a rate of C/12 in the voltage range of 1.5–4.0 V (1C refers to the theoretical capacity of 295 mAh g^{-1} calculated considering 2 K ions insertion). During the first potassiation process, a short slope is observed until around 1.8 V, followed by a sloped plateau at about 1.7 V. In contrast, only one slope appears up to 4.0 V in the first depotassiation process. During the second cycle, only sloped curves can be observed, while a pair plateau at 2.6 V/2.85 V can be seen in the 5th cycle for the potassiation/depotassiation processes, respectively. V_2O_5 nanoparticles deliver an initial potassiation/depotassiation capacity of 200 mAh g^{-1}/217 mAh g^{-1}. While the potassiation corresponds to the insertion of 1.36 K$^+$ per formula unit, the increased depotassiation capacity might be due to the decomposition of the electrolyte with the formation of the "cathode electrolyte interphase" (CEI) (Fig. S2) and some other irreversible side reactions, where CEI terminology is widely used for the positive electrode side now [26–28]. In the subsequent potassiation (second cycle) the material delivers only 120 mAh g^{-1} and
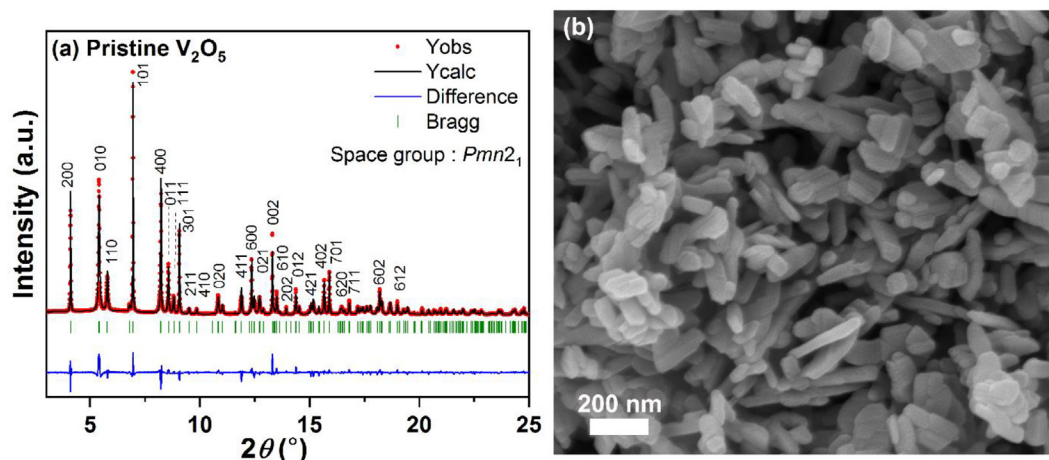
Fig. 1. Rietveld refinement based on synchrotron diffraction data (a) and SEM images (b) of V_2O_5 nanoparticles.
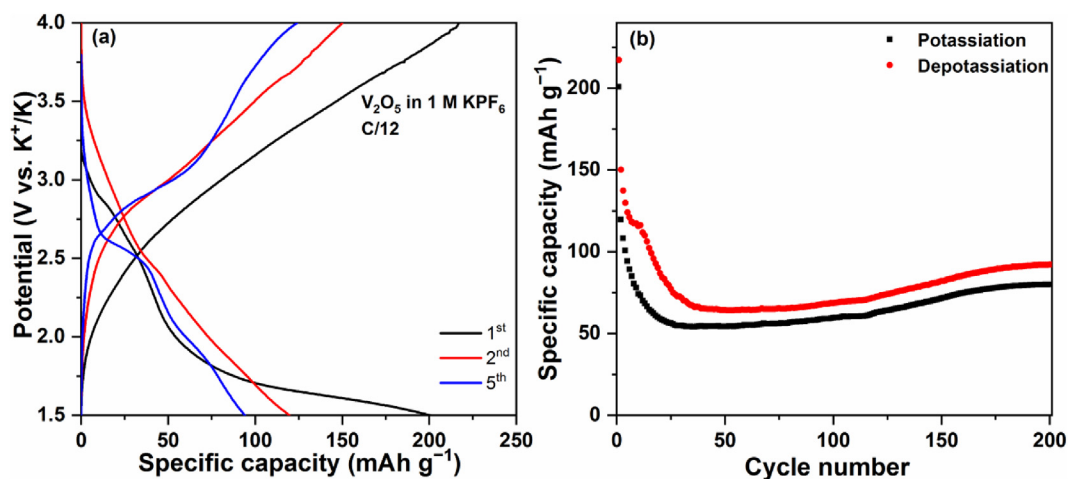

Fig. 2. Potassiation-depotassiation profiles (a) and cycling property (b) of V_2O_5 nanoparticles in 1 M KPF_6/PC (C/12).

undergoes a continuous capacity loss down with only 94 mAh g^{-1} at the 5th cycle. The capacity reaches its lowest value of 54 mAh g^{-1} at the 31st cycle and then slowly increases up to 80 mAh g^{-1} at the 200th cycle, as shown in Fig. 2(b). The main reason for the decay could be due to the (partial) dissolution of V_2O_5, less formation of CEI (see XPS), the irreversibility of the materials, and side reaction during the cycling. In fact, the coulombic efficiency is low, which suggests the presence of parasitic side reactions. Understanding the cause of capacity increase with cycling is rather complicated and challenging since it depends on many factors and interplay of components present in the cell. We have tried to improve the cycling performance of V_2O_5 by adding an additive fluoroethylene carbonate (FEC) to the electrolyte. V_2O_5 only shows a limited initial potassiation/depotassiation capacity of ~110/51 mAh g^{-1} with a large initial irreversible capacity. In the presence of FEC additive, the V_2O_5 electrode shows better cycling stability and improved coulombic efficiency (close to 100% of coulombic efficiency after 5 cycles) but rather low and unsatisfying reversible capacity during 60 cycles compared with that in KPF_6/PC as shown in Fig. S3. The stabilization can be due to a suppression of side reactions, which can arise from the interaction between the electrolyte and the highly reactive K metal which is used as coun-

ter and reference electrode. A similar stabilization effect by FEC is also observed with Na metal in NIBs [29]. In our group, Pfeifer et al. [30] demonstrated that metallic sodium can strongly react with organic carbonate-based electrolytes in Na-ion batteries and strongly affect their electrochemical performance of the investigated electrode material. In the same line, in order to understand if some kind of decomposition reactions occur in presence of metallic K, a preliminary experiment was done by adding K metal to both KPF_6/PC and KPF_6/PC + FEC. A massive color change is observed when K is immersed in KPF_6/PC along with the storage time (Fig. S4). The K metal changes to slight purple after 2 min and dark-earth purple (2 h) and finally to black-purple (21 h) in KPF_6/PC, indicating strong reactions occurring between K metal and KPF_6/PC electrolyte, which can cause strong side reaction for V_2O_5 electrode during cycling. The clear solution of KPF_6/PC turns to yellow after 21 h, while the solution of KPF_6/PC + FEC does not show many changes. This experiment indicates that FEC could form a protective layer on the surface of metallic K (in a similar way as for Na). The interphase of K metal and the composition of electrolytes can play a very important role on the performance of batteries. However, detailed investigations are out of the scope of this work.
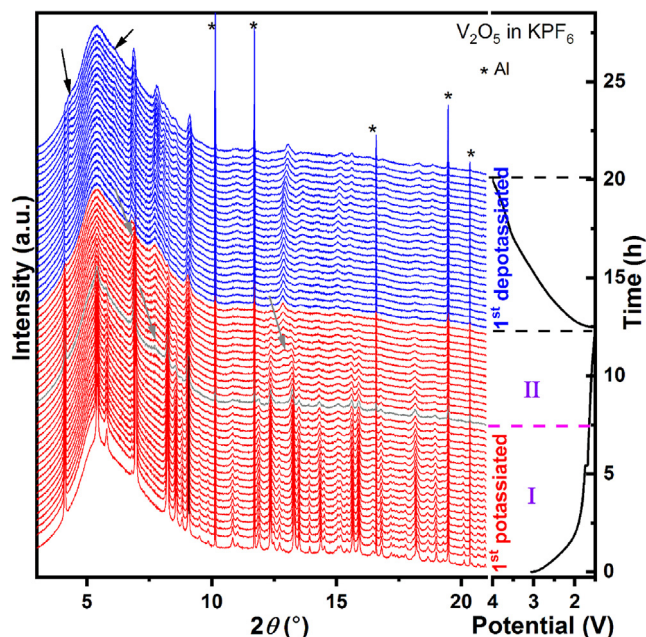
Fig. 3. *In operando* synchrotron diffraction from V_2O_5 during the first K-insertion/-extraction cycle and the corresponding voltage profile at a rate of C/15 (cell was running at C/30 for the first 5.4 h) indicating Region I, Region II and depotassiation.

3.3. Electrochemical mechanism

In order to elaborate the electrochemical storage mechanism upon K ions insertion and extraction in V_2O_5, *in operando* synchrotron diffraction was performed during the potassiation/depotassiation processes as shown in Fig. 3. Before potassiation, all reflections, except those marked with asterisk related to the Al current collector, could be assigned to the orthorhombic α-V_2O_5 phase (crystallized in space group $Pmn2_1$, see Fig. S5 for the Rietveld refinement of pristine α-V_2O_5). At the beginning of the 1st potassiation, some reflections of α-V_2O_5, such as 5.41° (010), 6.96° (101), 8.58° (011), 9.07° (301), 13.30° (002), 13.94° (202), 14.37° (012), 15.66° (312), and 15.90° (701) (enlarged 2 theta ranges are shown in Fig. 4), gradually shift to lower angles, indicating a solid solution
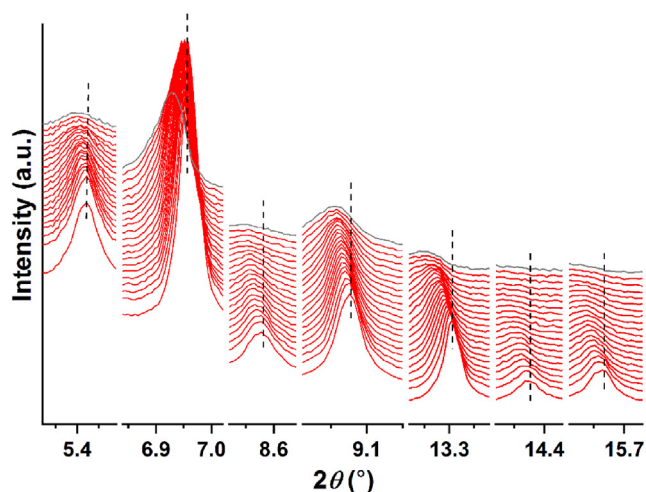
Fig. 4. Synchrotron diffraction with enlarged 2θ ranges of Region I selected from V_2O_5.

process with an expansion of the unit cell and the formation of solid solution phase up to $K_{0.6}V_2O_5$ (Region I with a capacity of 89 mAh g^{-1}, 1.65 V). Meanwhile, the intensity of reflections related to α-V_2O_5 continuously decreases and some reflections disappear along with K ions insertion (Region I). In contrast, other reflections such as 4.11° (200), 5.79° (110), 6.80° (210), 8.24° (400), 8.82° (111), 9.86° (410), 10.85° (020), 11.04° (120), 12.37° (600), and 13.51° (610), stay at the same position and their intensities also slowly reduce in Region I. During the solid solution reaction in Region I, the lattice parameter a shows minor changes (see Fig. S6), while lattice parameters b and c exhibit a significant increase. This is attributed to the insertion of large radii of K$^+$ in α-V_2O_5 host, extending the interlayer distance (b direction) and c direction. The a axis is parallel to the zigzag chains of conner-shared VO_5 pyramids and the structure cannot be strongly compressed or expanded in the direction a axis due to the hard frame of zigzag chains along the direction of a axis. Along with further K ions insertion (1.65 V, Region II), the shifted reflections obtained in Region I continuously shift to lower angles/stay at the same positions, while three new broad reflections, 6.78°, 7.75°, and 12.86° (pointed out by grey arrows, belong to new phase Ph1), appear and their intensities slowly increase until the end of the first potassiation at 1.5 V, indicating coexistence of a two-phase transition and a solid solution. Among them, the reflection at 7.75° emerges after insertion of 0.6 mol of K$^+$ per mol V_2O_5 (89 mAh g^{-1}). At the end of potassiation at 1.5 V (189 mAh g^{-1}), most of the reflections from $K_{0.6}V_2O_5$ disappear and only some broad reflections (K_x-V_2O_5, x = 1.28) can be observed (see the diffraction pattern of the potassiated state at 1.5 V in Fig. S7, 69th pattern). This might be attributed to the dissolution of V_2O_5 into the electrolyte or the formation of a $K_xV_2O_5$ compound with low crystallinity [31]. The dissolution of V_2O_5 into the electrolyte is confirmed by the color changes of separator above and inductively coupled plasma optical emission spectrometry (ICP-OES) result (Table S4). In addition, the two-phase transition reaction is not completed at the end of potassiation at 1.5 V. Le Bail refinement demonstrates that the reflections at the fully potassiated state consist of $K_{0.6}V_2O_5$ and a new phase Ph1 with lattice parameters a = 11.107 Å, b = 8.940 Å, and c = 3.233 Å, in space group $Pmn2_1$ (Fig. S8, $K_xV_2O_5$ is the average formula of two phases $K_{0.6}V_2O_5$ and a new phase Ph1). During the 1st depotassiation, three different features can be observed. Two broad new reflections at 4.13° and 6.11° emerge (pointed out by black arrows in Fig. 3) and their intensities increase, while some reflections, such as 6.79°, 6.90°, 7.73°, 8.04°, 9.03°, 12.85°, 13.56°, and 15.01°, shift to higher angles and slightly grow up. Additionally, other small broad peaks almost keep unchanged. It indicates that, upon K ions extraction from the structure, the K_xV_2-O_5 material undergoes a two-phase transition process accompanied with a solid solution. Le Bail refinement demonstrates that the reflections at the depotassiated state (4.0 V, $K_yV_2O_5$) are related to $K_{0.6-\delta}V_2O_5$ and a phase Ph2 with lattice parameters a = 11.128 Å, b = 8.761 Å, and c = 3.226 Å, in space group $Pmn2_1$ (Fig. S9, $K_yV_2O_5$ is the average formula of two phases $K_{0.6-\delta}V_2O_5$ and Ph2). The phase evolution of α-V_2O_5 during the 1st cycle is summarized as Scheme 1. Note that the lattice parameters of new phase Ph1 and Ph2 are similar to that of V_2O_5 with a doubling of the b-axis. Unfortunately, Ph1 and Ph2 cannot relate to any K-V_2O_5 based known phases and it is not possible to determine the structure neither of the new phases formed Ph1 at the end of potassiation nor of Ph2 at the end of the depotassiation. The reflections do not return to their initial positions of pristine V_2O_5, indicating irreversibility during the first K insertion/extraction (see Fig. S7). V_2O_5 displays a different reaction mechanism upon K-ions insertion from what is known for Li-ions insertion, where α-, ε-, δ-, γ-, and ω-phase can be observed depending on the amount of inserted Li-ions (x) [32]. Particularly, the α-phase (x < 0.1) and ε-phase
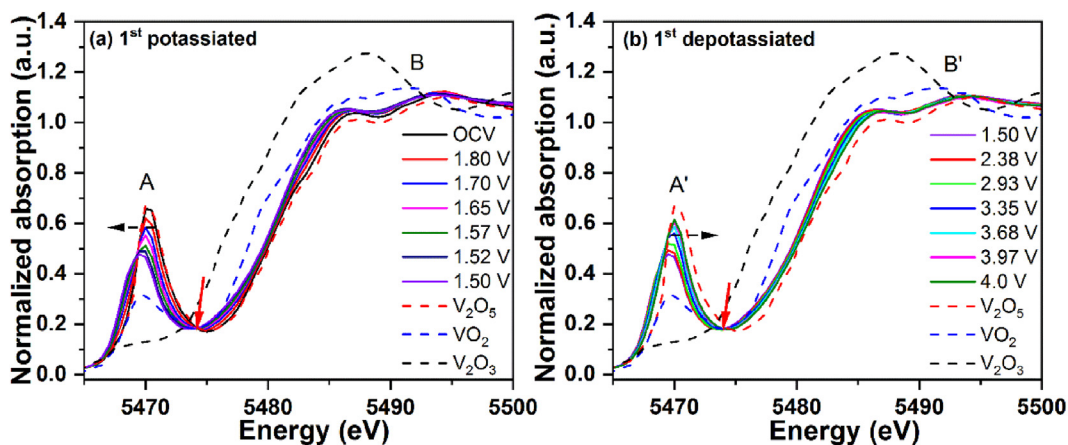
Scheme 1. Phase changes of V_2O_5 during the 1st cycle.

Fig. 5. *In operando* V *K*-edge XANES spectra during the 1st cycle in 1 M KPF$_6$; the isosbestic points are indicated by red arrows, the shifts of the pre-edge peak energies by black arrows.

(0.35 < x < 0.7) are fully reversible and the δ-phase is observed when x is 1 for Li$_x$V$_2$O$_5$. An irreversible transformation of δ-phase into γ-phase is observed for x > 1, and the γ-phase can be reversibly cycled in the range of $0 \leq x \leq 2.0$ while maintaining the γ-type structure. The irreversible formation of ω-phase with a rocksalt-type structure emerges upon the third lithium insertion into the V_2O_5 structure. Note that the particle size of V_2O_5 in our work is in a wide range of 50–200 nm, which would improve the capacity of materials because of its specific area and short K-ion migration. The reaction mechanism could change when the materials are changing from bulk size to nano-size. Particle size and charge/discharge rates will strongly affect the capacity of materials and the amount of inserted K ions and therefore have a significant influence on the observed synchrotron diffraction result. For example, nanostructuring of MoS_2 suppresses the 1T-triclinic phase transition and shortens Li-ion diffusion path lengths, allowing MoS_2 nanocrystal assemblies to behave as nearly ideal pseudocapacitors [33].

In operando XAS was performed on the V_2O_5 positive electrode material to probe the electronic and structural environments of V-ions during the electrochemical process. As displayed in Fig. 5, the edge position of the V K-edge spectrum for the initial state is slightly lower than that of the reference V_2O_5 spectrum, where V_2O_5, VO_2, and V_2O_3 are referred as standard materials with +5, +4, and +3 oxidation states, respectively. Hence, it can be confirmed that the oxidation state of V is mainly +5 in the initial state, in good agreement with XPS results discussed later. Moreover, an intense pre-edge peak on XANES data is observed for the V K-edge of pristine V_2O_5, which is due to the transitions from 1s to bound p-hybridized d-states [34,35] with the loss of centrosymmetry of the occupied V site. Indeed, the orthorhombic crystal structure of V_2O_5 is composed of square pyramids [VO$_5$] layers that share corners and edges and the V-ions are five-fold coordinated by oxygens in a distorted tetragonal pyramid.

During the first potassiation, the position (energy) of the V K-edge continuously shifts to lower energy, suggesting the reduction of vanadium ions accompanied by the K$^+$ insertion into the V_2O_5 structure. The energy of the V K-edge of the electrode potas-

siated to 1.5 V (x = 0.91 in K$_x$V$_2$O$_5$) is almost in the middle between that of standard VO_2 and V_2O_5 in good agreement with the electrochemical data (Fig. S10). One could also clearly see the shift from the first-derivative V K-edge XANES for the V_2O_5 during cycling (Fig. S11), indicating the reduction of the vanadium. Meanwhile, the pre-edge peak (A in Fig. 5(a)) slowly shifts to lower energy and its intensity gradually decreases, implying the reduction of the vanadium and the changes of the local V environments during K$^+$ insertion, owing to the co-existence of distorted tetragonal pyramids and centrosymmetric VO$_6$ octahedra. The intensity and the position of the pre-edge feature depend on the amount of inserted K ions. Along with the K ions insertion, the intensity of the pre-edge peak decreases. The position of the pre-edge peak shows a redshift because of an increase in symme-
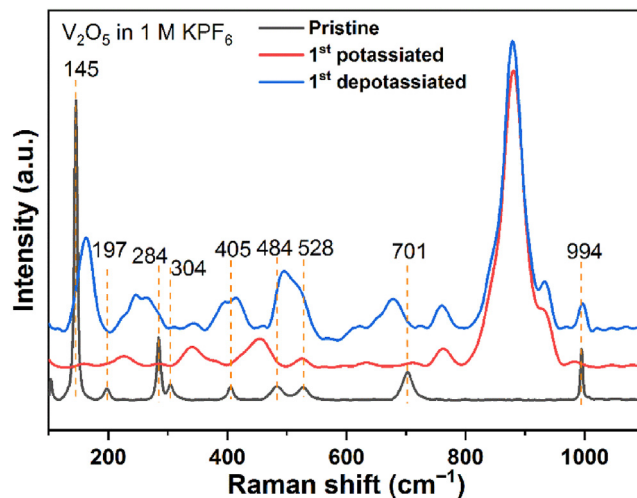

Fig. 6. Raman spectra of the pristine V_2O_5, the 1st potassiated V_2O_5, and the 1st depotassiated V_2O_5.

try and a decrease in the oxidation state. The increase in symmetry causes a decrease of the peak intensity due to the decreased probability of the 1s-3d transition [36]. The distorted tetragonal pyramids tend to change into less distorted VO_6 octahedra. This also lessens the Jahn-Teller distortion of the V-O octahedral units, which become more regular in shape [37]. Moreover, the V K-edge pre-edge centroid as a function of potential shows the energy changes along with cycling, in agreement with the edge shift above (Fig. S12), where similar plots have been shown by Banerjee et al. [38]. The edge resonance (B and B′ in Fig. 5), which is related to the energy absorption by core electrons [35,39] does not show remarkable changes in both shape and intensity. The reduction of V_2O_5 upon K insertion is quite different from the observations upon Mg insertion in the same material [40]. Upon

Mg insertion, significant changes in both shape and intensity of the edge resonance can be observed [40]. Furthermore, only one distinct isosbestic point [41] (red arrows in Fig. 5(a)) is obtained at ~5474 eV energy during the potassiation process, implying the occurrence of a two-phase reaction upon K ions insertion into the V_2O_5. Note that isosbestic point is commonly observed in XAS spectra and its presence implies that only two species contribute to the absorption around the isosbestic point with changing fractions of their concentration in the mixture [42–44]. This result is fully consistent with the conclusions from *in operando* synchrotron diffraction (Fig. 3).

During the first depotassiation, both the energy of the V K-edge and the pre-edge peak (A′ in Fig. 5(b)) exhibit a reversible behavior and shift to higher energy, indicating the progressive oxidation of V
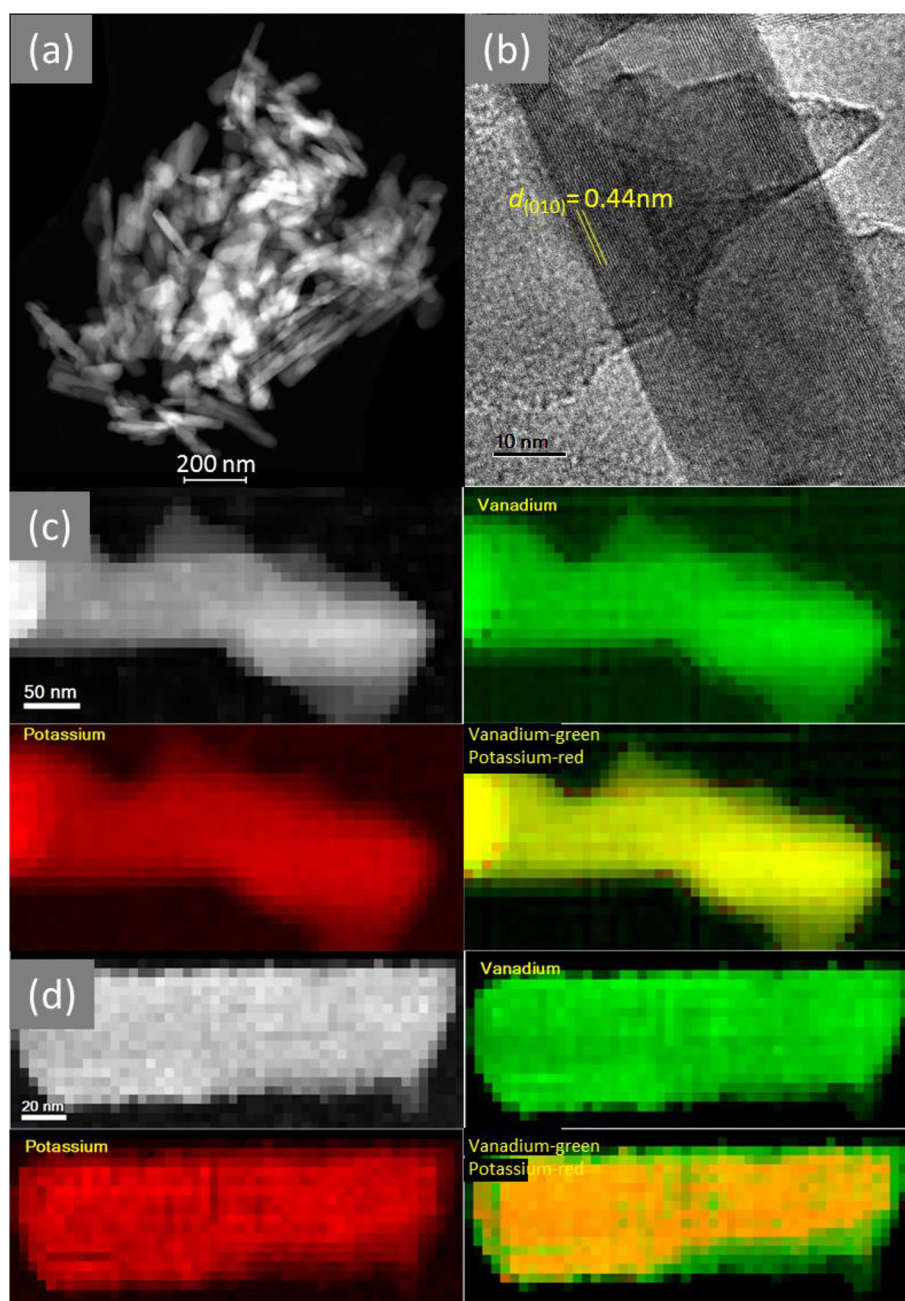
Fig. 7. STEM-HAADF and high-resolution TEM images of the pristine V_2O_5 (a and b), elemental mapping based on STEM-EELS spectrum imaging of K and V for the 1st potassiated V_2O_5 (c), and the 1st depotassiated V_2O_5 (d).

in the material during depotassiation. The intensity of the pre-edge peak continuously increases during K-ions extraction from the material, indicating a symmetry reduction at the V ions site. Moreover, one distinct isosbestic point (red arrows in Fig. 5(b)) is also obtained at ~5474 eV energy during the depotassiation process, indicating a two-phase reaction upon K-ions extraction from the structure. However, the energy of V K-edge and pre-edge peak at the potential of 4.0 V do not return to their initial energies but are slightly lower than that of pristine V_2O_5, which is consistent with *in operando* synchrotron diffraction and indicates an irreversible process.

To further study the short-range structure of the samples during K-ions insertion/extraction, Raman spectra were collected, as shown in Fig. 6 and Table S5. In the pristine orthorhombic V_2O_5 oxygen atoms occupy four distinct sites in a $[VO_5]$ pyramid unit, denoted as O(1)–O(4). The stretching mode of the V–O(1) bond is located at 994 cm^{-1} while its bending vibrations are located at 405 and 284 cm^{-1}. Raman peaks at 484 and 700 cm^{-1} are attributed to the bending vibration of the V–O(3) and the stretching vibration of the V–O(2), respectively. The peaks at 528 and 304 cm^{-1} are assigned to the stretching and bending vibrations, respectively, of the V–O(4) bond. The peaks at lower wavenumbers, 197 and 145 cm^{-1} are attributed to the atoms oscillating along the x-axis and the shear motion and rotations (along their axes) of the ladders, respectively. These results are consistent with previous work [45,46]. After K-ions insertion (1st potassiation), significant changes can be observed and some peaks related to V_2O_5 at 994, 528, and 284 cm^{-1} become weak and broad, while those at 701, 304, and 284 cm^{-1} completely disappear, while some broad and distinct new peaks appear at 226, 340, 455, 763, 880, and 931 cm^{-1}. Similarly, these significant changes in Raman spectra are also observed after Mg-ions insertion in V_2O_5 [40]. Hence, these new peaks might be ascribed to the new phase of $K_xV_2O_5$, where the broad peaks are probably attributed to the disordered local structure in the $K_xV_2O_5$ phase. It can be deduced that K ions are inserted into the interlayer of V_2O_5 crystals and bonded with oxygen atoms ($[KO_6]$ octahedra) in the V_2O_5 structure to form the K-rich $K_xV_2O_5$ phase. After K ions extraction ($K_yV_2O_5$), some new peaks, observed at 763, 880, and 931 cm^{-1}, still remain at the same position and several additional broad peaks can be observed between 200 and 700 cm^{-1}. This suggests that $K_xV_2O_5$ and $K_yV_2O_5$ have similar structure and the existence of a second phase in the depotassiated samples is confirmed. The appearance of peaks at 163 and 996 cm^{-1} indicates the existence of a layered structure similar to that of pristine V_2O_5. However, the material cannot return back to the initial state of V_2O_5 after K-ions extraction. These results confirm that K-ions insertion leads to the formation of a new $K_xV_2O_5$ phase. This transformation is only partially reversible during the following extraction of K-ions in the first cycle as identified by *in operando* synchrotron diffraction and XAS.

The morphology and the elemental distribution of potassium inside the V_2O_5 framework are studied by scanning transmission electron microscopy coupled with EELS spectrum imaging. Fig. 7 (a) displays a representative STEM-HAADF image of the pristine V_2O_5 sample. The initial morphology of the sample includes an uneven nanoparticle shape as well as a wire-like one, both in the nano-size range (around 50–200 nm) and in good agreement with SEM result. The high-resolution TEM image presented in Fig. 7(b) shows a highly crystalline sample with an interplanar distance of 0.44 nm corresponding with the (010) plane of the orthorhombic V_2O_5. Fig. 7(c) provides the elemental maps of K and V based on the STEM-EELS spectrum imaging of the potassiated sample. It proves a uniform distribution of K inside the V_2O_5 matrix. This result implies that some of the K-ions still remain in the structure
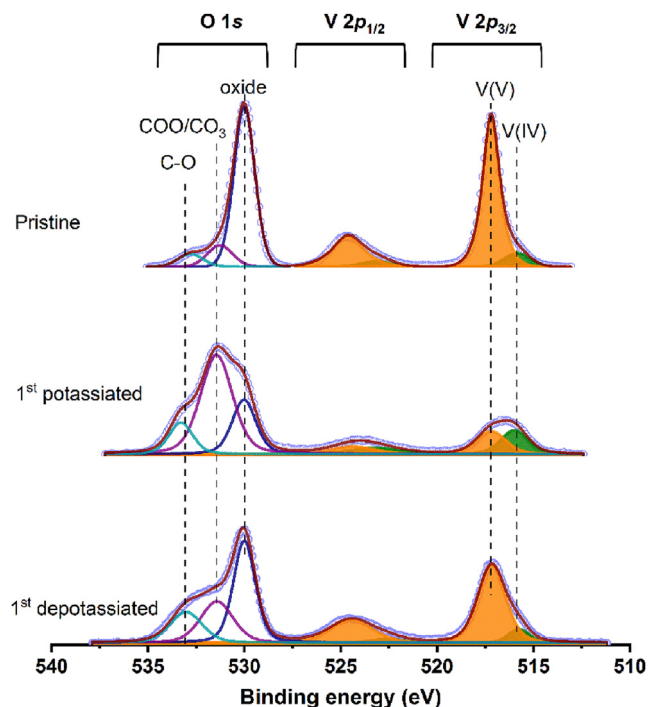

Fig. 8. V 2p and O 1s X-ray photoelectron spectra of the pristine V_2O_5, the 1st potassiated V_2O_5, and the 1st depotassiated V_2O_5.

after depotassiation (Fig. 7(d)) and, therefore, confirms the irreversibility of K-insertion into V_2O_5 during cycling.

The surface chemistry and surface elemental composition of pristine V_2O_5, of the first potassiated V_2O_5, and of the first depotassiated V_2O_5 were investigated using X-ray photoelectron spectroscopy. According to Fig. 8, the V 2p spectra of all three samples can be fitted with two doublets: one with V 2$p_{3/2}$ at 517.2 eV and the other one with weak intensity at 515.9 eV [47], which refer to the oxidation states of vanadium +5 and +4, respectively. This indicates that V exists mainly in the oxidation state +5 with an average oxidation state of +4.9. The O 1s spectra of all three V_2O_5 samples can be fitted with 3 peaks at 533.0, 531.4, and 530.0 eV, which correspond to the C–O and COO/CO$_3$, as well as V–O groups [48,49], respectively. In the pristine V_2O_5, the minor V(IV) could be assigned to the reduction of residual surfactant P123 during synthesis. The V 2p spectrum in the potassiated state could be fitted with 1.8 at% V(V) at 517.0 eV and 1.2 at% V(IV) at 515.9 eV with an oxidation state of +4.6 (about 55 at% carbon, 26 at% oxygen, 11 at% potassium, and 5 at% F), while the V 2p spectrum of the depotassiated state shows two V 2$p_{3/2}$ components at 517.2 with 3.5 at% V(V) and 515.8 eV with 0.5 at% V(IV), returning back to its initial oxidation state of +4.9. In short, some of the V (V) is reduced to V(IV) during the electrochemical potassiation and then, partially oxidized upon electrochemical depotassiation, which is consistent with the above Raman, TEM, and *in operando* results. Furthermore, COO/CO$_3$ and C–O detected in the pristine V_2O_5 could be due to the residual surfactant symmetric triblock copolymer P123 used during synthesis, where FTIR was performed to further confirm their existence (Fig. S13). After potassiation, the COO/CO$_3$:V–O ratio significantly increases compared to that of pristine V_2O_5, indicating the formation of a CEI on the positive electrode particles. Upon depotassiation, the COO/CO$_3$:V–O ratio decreases, but cannot return to the initial state, identifying the

decomposition or destruction of the CEI film on the particles. Therefore, some of the recorded capacity is due to the film formation/decomposition and the other part is due to potassium insertion/deinsertion.

4. Conclusions

Orthorhombic α-V$_2$O$_5$ nanoparticles were prepared via a hydrothermal approach. In the 1 M KPF$_6$/PC electrolyte, V$_2$O$_5$ nanoparticles deliver an initial potassiation/depotassiation capacity up to 200 mAh g^{-1} (1.36 K$^+$)/217 mAh g^{-1} in the potential range of 1.5–4.0 V with a rate of C/12. The electrode shows a rapid capacity loss and exhibits the lowest capacity of only 54 mAh g^{-1} at the 31st cycle. After that, the capacity slowly increases up to a value of 80 mAh g^{-1} at the 200th cycle. The storage mechanism upon K ions insertion into V$_2$O$_5$ is elucidated by *in operando* synchrotron diffraction and *in operando* XAS together with *ex situ* Raman, XPS, and TEM. Nano-V$_2$O$_5$ can act as a host for the electrochemical insertion and extraction of K-ions. The K-insertion/extraction mechanism in α-V$_2$O$_5$ differs from the ones for Li- and Mg-insertion/extraction because of the larger size of K ions. V$_2$O$_5$ undergoes a solid solution to form K$_{0.6}$V$_2$O$_5$ phase and then, upon further K ions insertion, goes through coexistence of a solid solution and a two-phase reaction. The coexistence of a two-phase and a solid solution mechanism reflects significant deviations from equilibrium, probably due to kinetic barriers and transport limitations. In addition, significant side reactions are indicated by the formation and destruction of a CEI, which might play a peculiar role in the degradation mechanism. Several strategies can be used to depress capacity fading such as carbon coating of electrode materials, additive for electrolytes, and producing stable passivation film on K anode. This approach helps to understand the mechanism occurring in electrode materials and benefits the development of KIBs towards improved electrochemical performance.

Declaration of Competing Interest

The authors declare that they have no known competing financial interests or personal relationships that could have appeared to influence the work reported in this paper.

Acknowledgments

References

[1] B. Dunn, H. Kamath, J.-M. Tarascon, Science 334 (2011) 928–935.
[2] J. Liu, Adv. Funct. Mater. 23 (2013) 924–928.
[3] A. Eftekhari, J. Power Sources. 126 (2004) 221–228.
[4] J.Y. Hwang, S.T. Myung, Y.K. Sun, Adv. Funct. Mater. 28 (2018) 1802938.
[5] S. Komaba, T. Hasegawa, M. Dahbi, K. Kubota, Electrochem. Commun. 60 (2015) 172–175.
[6] M. Okoshi, Y. Yamada, S. Komaba, A. Yamada, H. Nakai, J. Electrochem. Soc. 164 (2017) A54–A60.
[7] Y. Hamon, T. Brousse, F. Jousse, P. Topart, P. Buvat, D.M. Schleich, J. Power Sources 97–98 (2001) 185–187.
[8] M.N. Obrovac, V.L. Chevrier, Chem. Rev. 114 (2014) 11444–11502.
[9] Z.L. Jian, W. Luo, X.L. Ji, J. Am. Chem. Soc. 137 (2015) 11566–11569.
[10] J.D. Zhang, T.T. Liu, X. Cheng, M.T. Xia, R.T. Zheng, N. Peng, H.X. Yu, M. Shui, J. Shu, Nano Energy 60 (2019) 340–361.
[11] X. Zou, P. Xiong, J. Zhao, J. Hu, Z. Liu, Y. Xu, Phys. Chem. Chem. Phys. 19 (2017) 26495–26506.
[12] M. Clites, J.L. Hart, M.L. Taheri, E. Pomerantseva, ACS Energy Lett. 3 (2018) 562–567.
[13] L. Deng, X. Niu, G. Ma, Z. Yang, L. Zeng, Y. Zhu, L. Guo, Adv. Funct. Mater. (2018) 1800670.
[14] Y.-H. Zhu, Q. Zhang, X. Yang, E.-Y. Zhao, T. Sun, X.-B. Zhang, S. Wang, X.-Q. Yu, J.-M. Yan, Q. Jiang, Chem 5 (2019) 168–179.
[15] B. Tian, W. Tang, C. Su, Y. Li, ACS Appl. Mater. Interfaces 10 (2018) 642–650.
[16] Y. Zhang, X. Niu, L. Tan, L. Deng, S. Jin, L. Zeng, H. Xu, Y. Zhu, ACS Appl. Mater. Interfaces 12 (2020) 9332–9340.
[17] F. Ye, D. Lu, X. Gui, T. Wang, X. Zhuang, W. Luo, Y. Huang, J. Materiomics 5 (2019) 344–349.
[18] S.-M. Bak, Z. Shadike, R. Lin, X. Yu, X.-Q. Yang, NPG Asia Mater. 10 (2018) 563–580.
[19] X.D. Zhao, X. Zhang, D.H. Wu, H.C. Zhang, F. Ding, Z. Zhou, J. Mater. Chem. A. 4 (2016) 16606–16611.
[20] D. Koch, V.V. Kulish, S. Manzhos, MRS Commun. 7 (2017) 819–825.
[21] F. Fauth, I. Peral, C. Popescu, M. Knapp, Powder Diffr. 28 (2013) S360–S370.
[22] K.L. Parry, A.G. Shard, R.D. Short, R.G. White, J.D. Whittle, A. Wright, Surf. Interface Anal. 38 (2006) 1497–1504.
[23] M. Herklotz, J. Weiss, E. Ahrens, M. Yavuz, L. Mereacre, N. Kiziltas-Yavuz, C. Drager, H. Ehrenberg, J. Eckert, F. Fauth, L. Giebeler, M. Knapp, J. Appl. Crystallogr. 49 (2016) 340–345.
[24] V. Shklover, T. Haibach, F. Ried, R. Nesper, P. Novák, J. Solid State Chem. 123 (1996) 317–323.
[25] J. Yao, Y. Li, R.C. Massé, E. Uchaker, G. Cao, Energy Storage Mater. 11 (2018) 205–259.
[26] S. Liu, D. Liu, S. Wang, X. Cai, K. Qian, F. Kang, B. Li, J. Mater. Chem. A. 7 (2019) 12993–12996.
[27] J.-N. Zhang, Q. Li, Y. Wang, J. Zheng, X. Yu, H. Li, Energy Storage Mater. 14 (2018) 1–7.
[28] Z. Zhang, J. Yang, W. Huang, H. Wang, W. Zhou, Y. Li, Y. Li, J. Xu, W. Huang, W. Chiu, Y. Cui, Matter. 4 (2021) 302–312.
[29] S. Komaba, T. Ishikawa, N. Yabuuchi, W. Murata, A. Ito, Y. Ohsawa, ACS Appl. Mater. Interfaces 3 (2011) 4165–4168.
[30] K. Pfeifer, S. Arnold, J. Becherer, C. Das, J. Maibach, H. Ehrenberg, S. Dsoke, ChemSusChem 12 (2019) 3312–3319.
[31] Z. Yu, L. Tetard, L. Zhai, J. Thomas, Energy Environ. Sci. 8 (2015) 702–730.
[32] Q. Liu, Y. Liu, C.-J. Sun, Z.-F. Li, Y. Ren, W. Lu, E.A. Stach, J. Xie, Electrochim. Acta 136 (2014) 318–322.
[33] J.B. Cook, T.C. Lin, H.-S. Kim, A. Siordia, B.S. Dunn, S.H. Tolbert, ACS Nano 13 (2019) 1223–1231.
[34] T. Tanaka, H. Yamashita, R. Tsuchitani, T. Funabiki, S. Yoshida, J. Chem. Soc. Faraday Trans. 84 (1988) 2987–2999.
[35] J. Wong, F.W. Lytle, R.P. Messmer, D.H. Maylotte, Phys. Rev. B 30 (1984) 5596–5610.
[36] S. Passerini, W.H. Smyrl, M. Berrettoni, R. Tossici, M. Rosolen, R. Marassi, F. Decker, Solid State Ion. 90 (1996) 5–14.
[37] P.N. Trikalitis, V. Petkov, M.G. Kanatzidis, Chem. Mater. 15 (2003) 3337–3342.
[38] L. Whittaker, T.-L. Wu, C.J. Patridge, G. Sambandamurthy, S. Banerjee, J. Mater. Chem. 21 (2011) 5580–5592.
[39] H.D. Yoo, Y. Liang, H. Dong, J. Lin, H. Wang, Y. Liu, L. Ma, T. Wu, Y. Li, Q. Ru, Y. Jing, Q. An, W. Zhou, J. Guo, J. Lu, S.T. Pantelides, X. Qian, Y. Yao, Nat. Commun. 8 (2017) 339.
[40] Q. Fu, A. Sarapulova, V. Trouillet, L. Zhu, F. Fauth, S. Mangold, E. Welter, S. Indris, M. Knapp, S. Dsoke, N. Bramnik, H. Ehrenberg, J. Am. Chem. Soc. 141 (2019) 2305–2315.
[41] X. Liu, D. Wang, G. Liu, V. Srinivasan, Z. Liu, Z. Hussain, W. Yang, Nat. Commun. 4 (2013) 2568.
[42] L. Zhang, D. Sun, J. Feng, E.J. Cairns, J. Guo, Nano Lett. 17 (2017) 5084–5091.
[43] X. Liu, J. Liu, R. Qiao, Y. Yu, H. Li, L. Suo, Y.-S. Hu, Y.-D. Chuang, G. Shu, F. Chou, T.-C. Weng, D. Nordlund, D. Sokaras, Y.J. Wang, H. Lin, B. Barbiellini, A. Bansil, X. Song, Z. Liu, S. Yan, G. Liu, S. Qiao, T.J. Richardson, D. Prendergast, Z. Hussain, F.M.F. de Groot, W. Yang, J. Am. Chem. Soc. 134 (2012) 13708–13715.

[44] X.-J. Wang, C. Jaye, K.-W. Nam, B. Zhang, H.-Y. Chen, J. Bai, H. Li, X. Huang, D.A. Fischer, X.-Q. Yang, J. Mater. Chem. 21 (2011) 11406–11411.

[45] R. Baddour-Hadjean, J.P. Pereira-Ramos, C. Navone, M. Smirnov, Chem. Mater. 20 (2008) 1916–1923.

[46] G. Gershinsky, H.D. Yoo, Y. Gofer, D. Aurbach, Langmuir 29 (2013) 10964–10972.

[47] G. Silversmit, D. Depla, H. Poelman, G.B. Marin, R. De Gryse, J. Electron. Spectros. Relat. Phenomena. 135 (2004) 167–175.

[48] L.G. P., C.D. G., R.B. D., Surf. Interface Anal. 17 (1991) 267-272.

[49] J. Świątowska-Mrowiecka, V. Maurice, S. Zanna, L. Klein, P. Marcus, Electrochim. Acta 52 (2007) 5644–5653.